

# Defect filtering for thermal expansion induced dislocations in III-V lasers on silicon

Cite as: Appl. Phys. Lett. **117**, 122101 (2020); doi: [10.1063/5.0023378](https://doi.org/10.1063/5.0023378)

Submitted: 29 July 2020 · Accepted: 4 September 2020 ·

Published Online: 21 September 2020



Jennifer Selvidge,<sup>1</sup>  Justin Norman,<sup>1</sup>  Eamonn T. Hughes,<sup>1</sup>  Chen Shang,<sup>1</sup> Daehwan Jung,<sup>2</sup>  Aidan A. Taylor,<sup>1</sup> M. J. Kennedy,<sup>3</sup> Robert Herrick,<sup>4</sup> John E. Bowers,<sup>1,3</sup> and Kunal Mukherjee<sup>1,a)</sup> 

## AFFILIATIONS

<sup>1</sup>Materials Department, University of California, Santa Barbara, California 93106, USA

<sup>2</sup>Korea Institute of Science and Technology, Seoul 02792, South Korea

<sup>3</sup>Electrical and Computer Engineering Department, University of California, Santa Barbara, California 93106, USA

<sup>4</sup>Intel Corporation, Santa Clara, California 95054, USA

<sup>a)</sup>Author to whom correspondence should be addressed: [kunalm@ucsb.edu](mailto:kunalm@ucsb.edu)

## ABSTRACT

Epitaxially integrated III-V semiconductor lasers for silicon photonics have the potential to dramatically transform information networks, but currently, dislocations limit performance and reliability even in defect-tolerant InAs quantum dot (QD)-based lasers. Despite being below the critical thickness, QD layers in these devices contain previously unexplained misfit dislocations, which facilitate non-radiative recombination. We demonstrate here that these misfit dislocations form during post-growth cooldown due to the combined effects of (1) thermal-expansion mismatch between the III-V layers and silicon and (2) mechanical hardening in the active region. By incorporating an additional sub-critical thickness, indium-alloyed “misfit dislocation trapping layer,” we leverage these mechanical hardening effects to our advantage, displacing 95% of misfit dislocations from the QD layer in model structures. Unlike conventional dislocation mitigation strategies, the trapping layer reduces neither the number of threading dislocations nor the number of misfit dislocations. It simply shifts the position of misfit dislocations away from the QD layer, reducing the defects’ impact on luminescence. In full lasers, adding a misfit dislocation trapping layer both above and below the QD active region displaces misfit dislocations and substantially improves performance: we measure a twofold reduction in lasing threshold currents and a greater than threefold increase in output power. Our results suggest that devices employing both traditional threading dislocation reduction techniques and optimized misfit dislocation trapping layers may finally lead to fully integrated, commercially viable silicon-based photonic integrated circuits.

Published under license by AIP Publishing. <https://doi.org/10.1063/5.0023378>

Silicon-based photonic integrated circuits are poised to dramatically increase the data network bandwidth and energy efficiency and enable chip-scale sensing, detection, and ranging. Direct epitaxial integration of III-V semiconductor lasers on silicon promises cost-efficiency and scalability,<sup>1</sup> but fabricating reliable, high-performance GaAs- or InP-based lasers on silicon is challenging.<sup>2–6</sup> The lattice constant mismatch between the substrate and III-V film generates threading dislocations (TDs) that rise upward through the film.<sup>4</sup> Where they intersect the device active region, they facilitate non-radiative recombination, degrading both performance and reliability.<sup>7,8</sup> While decades of work have reduced TD densities (TDDs) to  $10^6$ – $10^7$  cm<sup>−2</sup> (Refs. 9–11) and developed more dislocation-tolerant active materials such as InAs-quantum dots (QDs) in InGaAs quantum wells (QW) (dots in a well or DWELL),<sup>12–18</sup> commercially viable III-V lasers on silicon have yet to be realized.

We recently discovered an additional, key performance-limiting defect present in InAs QD lasers on silicon: unexpected misfit dislocations (MDs) lying along the upper and lower boundaries of the active region, even in record lifetime QD lasers.<sup>19,20</sup> These ⟨110⟩-oriented MDs, like TDs, limit performance and reliability because they, too, are potent non-radiative recombination centers.<sup>21</sup> Worse still, they may be far more damaging as they have a much larger interaction area with the active region. MDs normally form during growth in layers exceeding the critical thickness for dislocation glide;<sup>22</sup> to prevent this, the active layers in both QW and DWELL lasers are carefully designed to be below the critical thickness.<sup>23</sup> We do not appear to be the first to see MDs in lasers on silicon where the active region is nominally grown below the critical thickness. Groenert *et al.* observe unexpected ⟨110⟩-oriented MDs in QW-based devices grown on silicon via metal-organic chemical vapor deposition (MOCVD),<sup>6,24</sup> and Hasegawa *et al.*

report  $\langle 110 \rangle$ -oriented dark line defects in electroluminescence measurements on unaged GaAs-based QW layers on Si, consistent with the presence of MDs.<sup>8</sup> We acknowledge that there are a relatively few reports of MDs in QD lasers and tentatively attribute this to the practical difficulties of seeing them: QD strain contrast masks MD strain contrast in conventional cross-sectional transmission electron microscopy (XTEM).<sup>20</sup> Thus, MDs have seemingly gone unaddressed in these systems.

Here, we propose a formation mechanism for these MDs centered on the thermal expansion mismatch rather than the lattice mismatch and validate it in model structures and full DWELL lasers on silicon. We further demonstrate an unconventional MD filter that consists of thin mechanically hardened “trapping layers (TLs)” placed directly above and below the laser active region in the epitaxial stack. These layers displace MDs away from the QDs, rather than removing them entirely, an atypical filtering strategy that we show yields improvements comparable to an order of magnitude reduction in the TDD.

We first examine model structures using scanning electron microscopy (SEM)-based cathodoluminescence (CL) spectroscopy to directly observe the effects of MDs on DWELL emission. The trapping-layer-free “baseline” structure (described in Ref. 21) consists of a GaAs film with a single InAs DWELL layer 100 nm below the surface of a GaAs-on-Si template.<sup>21</sup> CL images were collected at room temperature on an Attolight Rosa at 10 kV. The CL map of the wetting-layer emission at 1005 nm [Fig. 1(a)] shows a network of  $\langle 110 \rangle$ -oriented dark lines and spots, corresponding to MDs and TDs, respectively. The sharp dark lines indicate that MDs lie sufficiently close to the QD layer to substantially lower light emission in their vicinity. The InAs QD ground-state luminescence map collected at 1245 nm [Fig. 1(b)] has the same dark features although they appear more diffuse.

The single DWELL layer is below the critical thickness, and so we hypothesize the MDs in this system form not during growth but during cooldown. Since GaAs has a larger thermal expansion coefficient than silicon ( $\alpha_{\text{GaAs}} - \alpha_{\text{Si}} \approx 3 \times 10^{-6} \text{ K}^{-1}$ ), GaAs layers, which are essentially unstrained by the end of growth at 540 °C, become up to 0.1% biaxially tensile strained during cooldown as they approach 300 °C. Due to this thermal strain, the still-mobile TD segments can glide in the GaAs layers thicker than just a few hundred nanometers. This is not surprising: we know that thermal stress can drive dislocation glide—thermal cyclic annealing (TCA) takes advantage of this very principle to reduce TDDs.<sup>25</sup> Even so, TDs gliding during cooldown is not inherently problematic. If, however, the indium-containing DWELL layer inhibits lateral TD motion,<sup>26</sup> as shown in Fig. 1(c), then as the free TD segment in the thick GaAs layer glides away, the TD segment in the DWELL is left behind, and a MD forms at the QD layer interface. We hypothesize that this mechanical hardening arises from uneven stress fields generated by the strained QDs<sup>27</sup> and alloy fluctuations in the  $\text{In}_{0.15}\text{Ga}_{0.85}\text{As}$  QW. The latter effect, similar to alloy hardening phenomena reported previously in bulk semiconductors,<sup>28,29</sup> occurs because the difference in covalent radii of indium (142 pm) and gallium (124 pm) generates in-layer stress fluctuations.<sup>30</sup> See the [supplementary material](#) (Fig. S1) for additional details. Finally, note that no TD glide (and thus no MD formation) occurs above the DWELL because the GaAs capping layer is too thin to relax.

If our proposed mechanism is correct, we should be able to leverage this hardening effect to displace the MDs from the DWELL layer. By inserting a 7-nm  $\text{In}_{0.15}\text{Ga}_{0.85}\text{As}$  “trapping layer” 100 nm below the

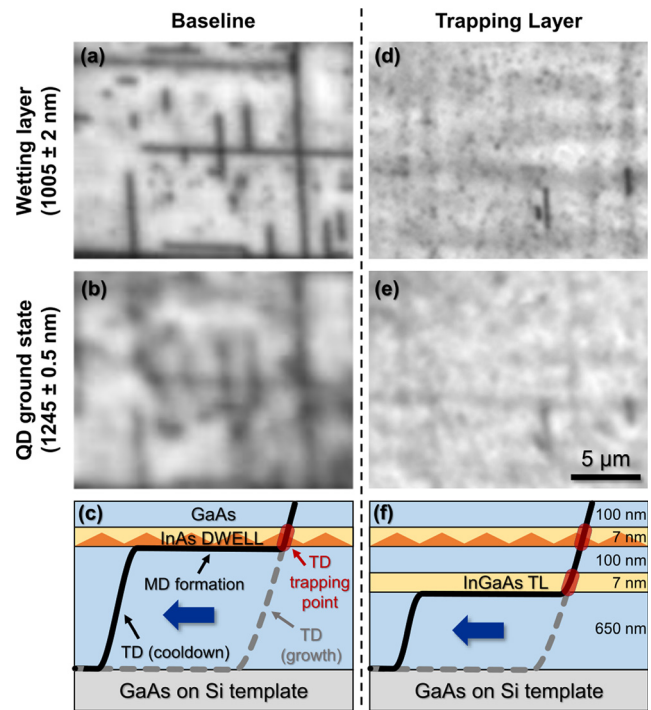


**FIG. 1.** (a) and (b) Monochromatic cathodoluminescence (CL) images of the baseline structure at (a) QD wetting-layer emission wavelength (1005 nm) and (b) QD ground-state emission wavelength (1245 nm). (c) Schematic representation of approximate dislocation evolution in the baseline structure. During cooldown, enough tensile stress builds in the thick GaAs layer below the QD layer for the threading dislocation (TD) to glide from its growth position (gray dotted line). The QD layer traps the TD (red box), causing a misfit dislocation (MD) to form at the bottom interface. The 100-nm GaAs cap is too thin to relax, and so no MD forms here. (d) and (e) Comparable CL of the trapping layer structure from (d) the wetting layer and (e) the QD ground state. The total dark line length in the DWELL layer is  $20\times$  lower than that in the baseline. (f) While the TD in the thick GaAs layer still glides in response to the tensile stress, by introducing an additional TD trapping point, the trapping layer displaces MD formation away from the QD layer.

DWELL, we can reduce the MD length at the DWELL layer by  $20\times$  [Figs. 1(d) and 1(e)]. The trapping layer itself should have a negligible impact on the TDD because it is below the critical thickness, and indeed, the measured TDD is comparable to that of the baseline structure. Instead, introducing an additional TD trapping point (red box) [Fig. 1(f)] forces TD glide and the resulting MD formation to occur below the trapping layer, rather than at the QDs. This agrees with the observed faint, broad dark lines that we attribute to MDs below the trapping layer. Assuming that the distance between the hardened layers is sufficiently small (i.e., intermediate GaAs is below the critical thickness induced by the thermal contraction), no MDs can form between the trapping layer and the DWELL. Just as with the DWELL, MDs cannot pass through the trapping layer due to the tensile-to-compressive strain reversal at this interface.

To gain more detailed insight into the structural evolution of MDs and TDs, we use a diffraction-based SEM technique, electron-channeling contrast imaging (ECCI), to directly observe a continuation of the MD formation process that occurs during cooldown at

room temperature (Fig. 2). Previous work has demonstrated that electron beams generate electron-hole pairs that recombine at dislocations and can drive dislocation glide in heteroepitaxial thin film semiconductors with sufficient residual stress,<sup>31,32</sup> as is the case in our system, as well as in bulk semiconductors with an externally applied stress.<sup>33,34</sup> Although glide processes cease below  $\sim 300^\circ\text{C}$ , the thermally induced tensile stress continues to build, and so the GaAs layers experience a 0.15% biaxial tensile strain at room temperature. Figure 2(a)—collected on a Thermo Fisher Apreo S SEM at 30 kV in the (400)/(220) channeling condition—shows a time-lapse evolution of a single TD in the baseline model structure. Initially, only a spot of point contrast is visible where the TD segment exits the film surface. Electron-beam irradiation supplies energy that reanimates TD glide,

so the free TD segment below the mechanically hardened QD-layer glides away, forming a MD that lengthens over time (orange arrows). We see no point contrast on the growing end, indicating that this end sinks down into the film beyond the detection range of ECCI, just as depicted in Fig. 1(c). If, instead, MDs formed due to the DWELL exceeding critical thickness, we would expect to see the upper TD segment gliding, but here, it is stationary. This provides direct evidence that our proposed mechanism—based on thermal strain buildup during cooldown and local TD trapping—drives MD formation.

Figures 2(b)–2(e)—collected on a FEI Quanta SEM under the same conditions as Fig. 2(a)—compare MD densities between the baseline and the trapping layer structure before and after heavy electron-beam irradiation. The as-grown baseline structure [Fig. 2(b)] contains MDs, marked with black arrows, following growth and cooldown. Based on the limited 100–200 nm depth sensitivity of ECCI, these sharp-contrast MDs must be reasonably near the film surface, most likely just below the shallow QD layer, as in Figs. 1(a)–1(c). Electron-beam irradiation causes additional sharp-contrast MD segments, marked with orange arrows, to form and grow [Fig. 2(c)]. In the as-grown trapping-layer structure [Fig. 2(d)], we measure a  $20\times$  reduction in the total shallow (high-sharpness) MD length from the baseline (over a  $2500\text{-}\mu\text{m}^2$  area), in agreement with CL. Electron-beam irradiation generates a high-density network of diffuse-contrast MD lines [Fig. 2(e)]. Their diffuse contrast indicates that these dislocations are located deeper in the structure, likely at the trapping layer.<sup>35</sup> Notably, the density of high-sharpness, shallow dislocations remains constant, indicating that SEM irradiation does not increase the MD length near the QD layer. As recombination-enhanced dislocation motion (REDM) processes are common failure mechanisms in semiconductor lasers, this is promising for laser reliability.

To investigate the efficacy of misfit trapping layers in full lasers, we fabricated InAs DWELL ridge structures on (001) Si with trapping layers in the epitaxial stack, shown schematically in Fig. 3(a), alongside a baseline sample with no trapping layers, both grown from the same  $3 \times 10^7 \text{ cm}^{-2}$  TDD buffer (see Refs. 11 and 36 for buffer and full laser growth details). All lasers were fabricated together into 3- $\mu\text{m}$  wide, 1500- $\mu\text{m}$  long, cleaved-facet, deeply etched ridge structures. Unlike with the model structures, the GaAs/AlGaAs layers above the active region here are sufficiently thick to relax during cooldown, enabling MD formation at both the uppermost and lowermost DWELLs, as seen in Ref. 20. To trap defects from both sides, we insert two sub-critical thickness 7-nm trapping layers 80 nm above and below the active region, composed of  $\text{In}_{0.15}\text{Ga}_{0.85}\text{As}$  and  $\text{In}_{0.15}\text{Al}_{0.85}\text{As}$ , respectively. These dissimilar alloys minimize electrical barriers due to band misalignment, but we expect them to have near-identical trapping ability. Since the covalent single-bond radii of aluminum (126 pm) and gallium (124 pm) are nearly identical, an equivalent indium alloying fraction should harden both layers similarly; note that these similar covalent radii also explain why the AlGaAs layers do not inhibit TD glide. Figures 3(b) and 3(c) show the effect of trapping layers on MD formation via bright-field (BF) on-zone ([100]) cross-sectional STEM. All STEM images were acquired using a Thermo Fisher Talos 200X G2 TEM/STEM (200 kV) with a standard BF STEM circular detector and a beam convergence angle of 10.5 mrad. The sample lift-out geometry, oriented at  $45^\circ$  to the orthogonal MD arrays [Fig. 3(b), inset], ensures that all MDs appear as equal-length horizontal lines. As shown in both low [Fig. 3(b)] and high [Fig. 3(c)] magnification

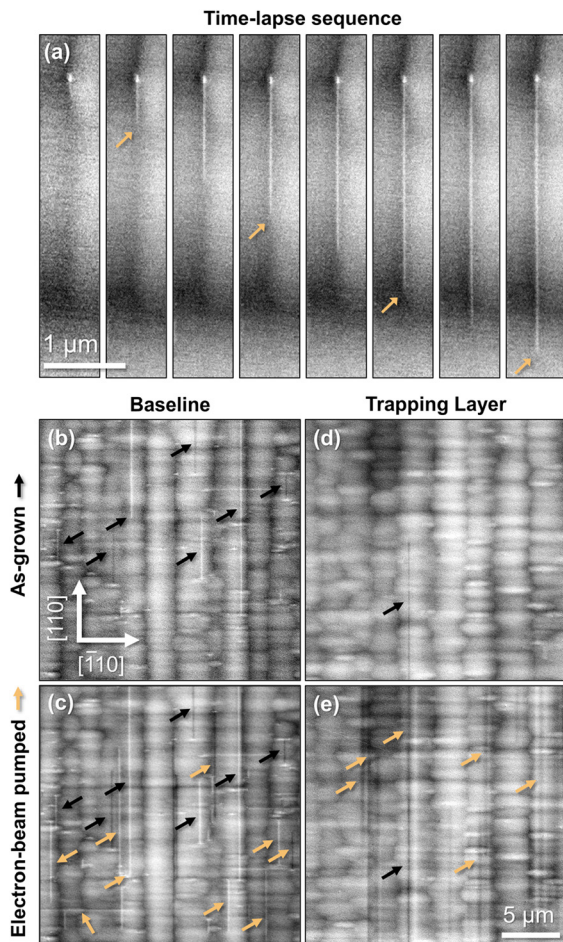


**FIG. 2.** (a)–(e) Electron-channeling contrast imaging (ECCI) of the baseline and trapping layer model structures. (a) ECCI time-lapse sequence ( $\sim 550$  s image interval) showing growth of a misfit dislocation (MD) (orange arrows) from a stationary, trapped threading dislocation (TD) segment in the baseline structure. (b) and (c) Corresponding ECCI of the baseline structure (b) before and (c) after electron-beam illumination. Black arrows indicate as-grown MD positions; orange arrows indicate MD growth from electron-beam pumping. (d) and (e) ECCI of the trapping layer structure (d) before and (e) after electron-beam illumination. Compared to the sharp line contrast of MDs in (b) and (c), the diffuse line contrast in (e) is due to MDs lying deeper in the structure, i.e., at the trapping layer.



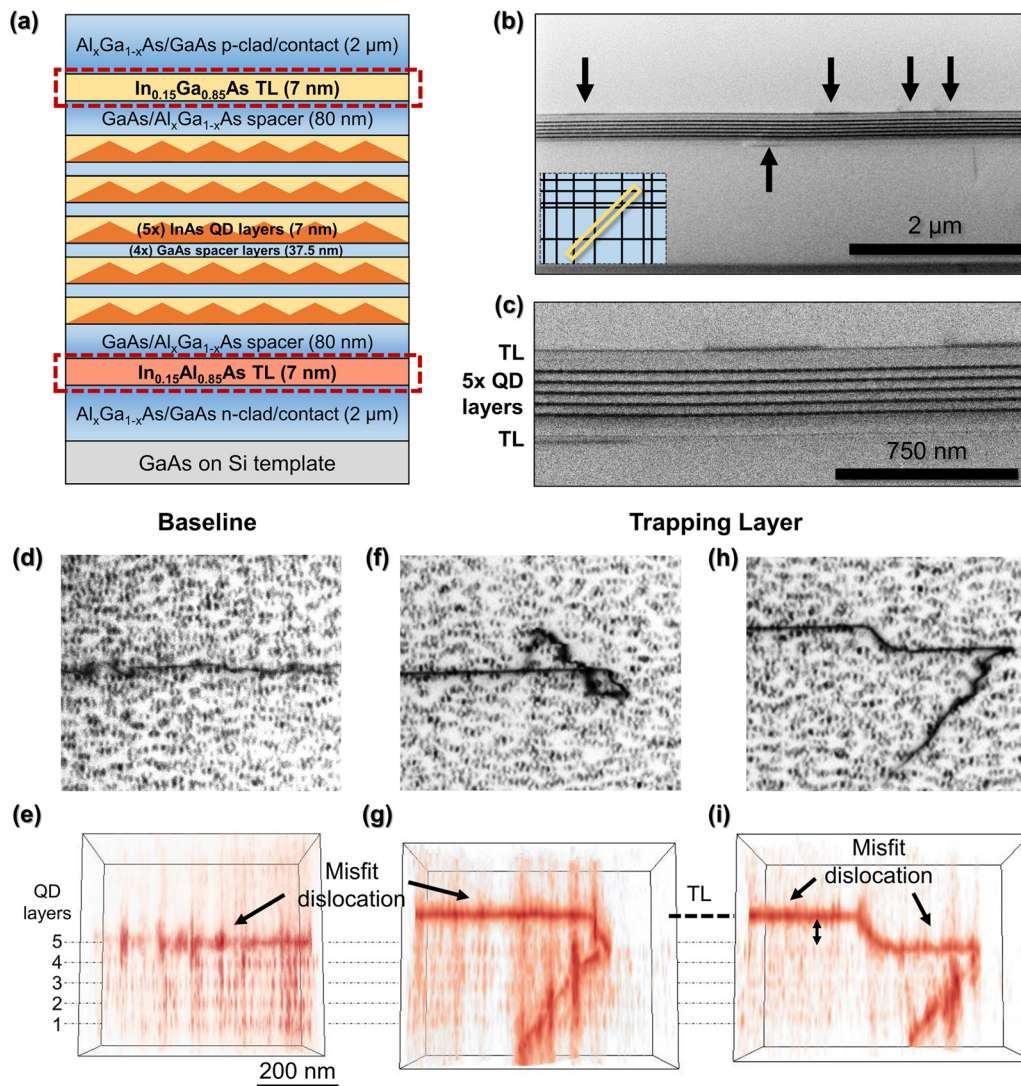


**FIG. 3.** (a) Schematic of a quantum dot (QD) laser with trapping layers (TLs) (red boxes) above and below the QD layers. Baseline samples are equivalent but lack trapping layers. (b) Cross-sectional bright-field (BF) STEM ([100] zone) of a trapping-layer laser. The inset shows the foil orientation relative to misfit dislocations (MDs). Arrows mark MD segments at the trapping layers. (c) High-magnification image of (b). (d) and (e) Baseline laser: (d) BF plan-view (PV)-STEM image ( $g = 220$ ) showing a MD among QDs. (e) Cross-sectional tomographic reconstruction showing the MD at the fifth QD layer. (f)–(i) Trapping layer laser: (f) BF PV-STEM showing a MD terminating in a threading dislocation (TD). (g) Reconstruction shows the MD lying at the trapping layer. (h) MDs at two heights with a TD end. (i) Reconstruction reveals a short MD at the top QD layer with the rest lying at the trapping layer.

images, MDs (black arrows) are displaced from the active region to the upper and lower trapping layers. Figure S2 provides additional evidence of misfit trapping in a full laser.

We illustrate the differences between the trapping layer and baseline structures using strain-contrast electron tomography generated from BF plan-view (PV)-STEM images taken across a  $\sim 60^\circ$  tilt range. Tomography is traditionally performed by tilting along a single axis, but here we followed the  $g = 220$  Kikuchi band using a double-tilt holder to maximize strain contrast and used the BF detector as a virtual aperture. A sample PV-STEM image for the baseline [Fig. 3(d)] shows a MD amid a field of QDs. The tomographic reconstruction [Fig. 3(e)], created using Tomviz (<https://tomviz.org>), resolves the five QD

layers and shows that this MD lies at the uppermost QD layer. In a trapping layer laser, Figs. 3(f) and 3(g) show a PV-STEM image and a tomographic reconstruction, respectively, of a MD and a terminating TD segment. Although strain-contrast tomography cannot resolve the trapping layer itself, the MD clearly lies away from the DWELL at the trapping layer's height. The TD forms no additional MD segments as it travels downward through the QD layers. Figure 3(h) also shows a PV-STEM image of a dislocation in a trapping layer laser, but here, there is a short, angled section along the MD, indicating a change in the height. The tomographic reconstruction [Fig. 3(i)] confirms that the MDs lie at the trapping layer and the uppermost QD layer. We expect that because the trapping-layer hardening effect arises from

alloy fluctuations, it is locally uneven. This can allow TDs to glide briefly until they reach a region with enough trapping to prevent further motion. This is explored further in Fig. S1. Unfortunately, this causes a MD to form at the outermost QD layer. Nevertheless, trapping layers displace the most MD length from the QDs as confirmed by PV-STEM (not shown).

Room temperature photoluminescence spectroscopy and continuous-wave (CW) light output-current-voltage (LIV) curves of a representative high performing device from both designs are shown in Figs. 4(a) and 4(b), respectively. Introducing trapping layers increases photoluminescence intensity by approximately  $2\times$  compared to the baseline [Fig. 4(a)]. This agrees with the marked improvements in threshold current, slope efficiency, and output power shown in the representative LIV curves [Fig. 4(b)]. Histograms comparing the structures along the same metrics [Figs. 4(c)–4(e)] further support these performance improvements. The trapping layer design shows a  $2\times$  reduction in median threshold current from the baseline. The lowest measured threshold current (16 mA) represents a 40% decrease from the baseline minimum. This is also 20% below identically designed state-of-the-art lasers on Si,<sup>36</sup> even with a  $4\times$  higher TDD here. We additionally observe an impressive 60% increase in median slope efficiency and a  $3.4\times$  increase in median peak single-facet output power for trapping

layer lasers. Finally, the median electrically dissipated power at rollover for trapping layer lasers (0.85 W) is approximately twice that of the baseline (0.46 W) (not shown). This indicates—assuming comparable thermal impedances—that the inclusion of trapping layers increases the lasers' optical amplification (gain). We cannot determine whether trapping layers adversely impact electrical transport in these lasers due to large variability in the series resistances across both sets of devices. But as higher-than-usual specific contact resistances across all devices ( $p$ :  $2.3 \times 10^{-5} \Omega\text{-cm}^2$ ,  $n$ :  $5.5 \times 10^{-5} \Omega\text{-cm}^2$ ) represent a limiting factor on output power, we anticipate that processing modifications will further improve device performance.

The relative performance improvements reported here—achieved simply by displacing existing MDs—are comparable to previous gains achieved by reducing the TDD by an order of magnitude ( $7 \times 10^7 \text{ cm}^{-2}$  to  $7 \times 10^6 \text{ cm}^{-2}$ ).<sup>37</sup> As device thicknesses are critical for many applications, it is highly advantageous that these performance gains made using thin misfit trapping layers compare favorably to those achieved using hundreds of nanometers of traditional TD filters. The same single order-of-magnitude reduction in the TDD also resulted in a nearly four order-of-magnitude increase in device lifetimes.<sup>37</sup> In these low TDD and low strain systems, the total active-region MD line length is determined by the TDD and glide kinetics,

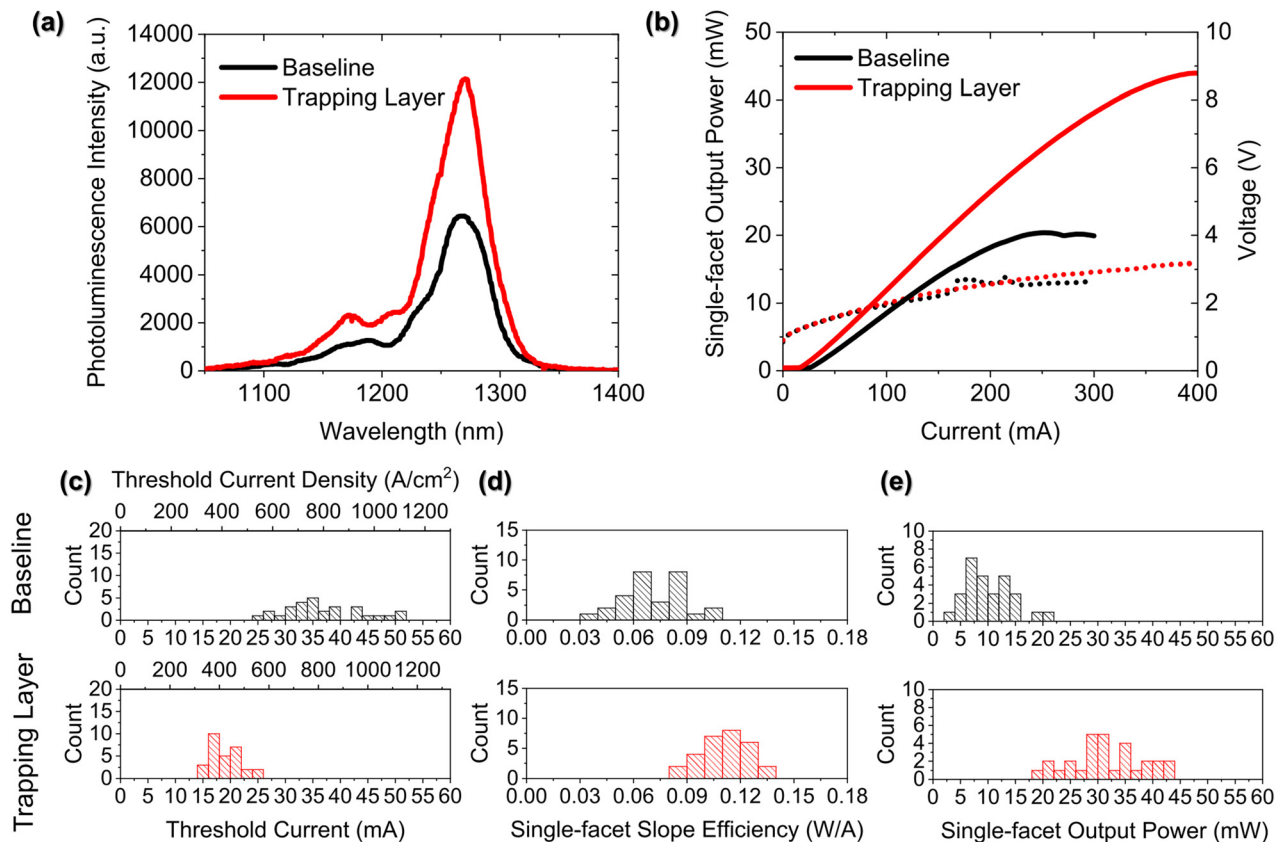


**FIG. 4.** (a)–(e) Comparison of baseline (black) and trapping layer (red) lasers. (a) Photoluminescence intensity comparison of trapping layer and baseline lasers. (b) Single-facet output power (mW) (solid) and voltage (V) (dashed) as a function of current (mA). A lower threshold current and higher slope efficiency and peak output power are observed in the trapping layer laser compared to the baseline. Current–voltage (IV) curves are comparable for both designs. (c)–(e) Histograms showing performance improvements of trapping layer devices along key performance metrics: (c) threshold current (mA), (d) slope efficiency (W/A), and (e) output power (mW).

and so this dramatic increase in the lifetime is likely explained in part by an unseen reduction in the total MD line length. All dislocation line length, whether MD or TD, within the active region degrades laser performance and lifetime; the inclusion and optimization of trapping layers thus complement important, ongoing TDD reduction efforts.<sup>38</sup> In future work, we will determine whether eliminating MDs enables epitaxially integrated InAs QD lasers to finally meet commercial lifetime requirements at an operating temperature of 60 °C.

In summary, we have proposed a mechanism that describes how **TDs give rise to highly damaging MDs that form during post-growth cooldown in certain epitaxial III–V-on-silicon structures.** We mitigate this by inserting thin mechanically hardened layers to locally inhibit TD glide and displace MD formation away from the QDs, removing 95% of the MD length in model structures. The trapping layers, placed both above and below the active region, represent a significant departure from traditional defect filtering: they displace, rather than remove, defects that form during cooldown, rather than during growth. For silicon photonics, this may finally clear the path to commercially viable, monolithically integrated, III–V-on-silicon photonic integrated circuits.

See the [supplementary material](#) (Fig. S1) a schematic representation of (a) the stresses a dislocation experiences in misfit trapping layer structures and a visualization of the approximate stress landscapes in the (b) In<sub>0.15</sub>Ga<sub>0.85</sub>As misfit trapping layer and (c) the QD layer and (Fig. S2) two tilted cross-sectional bright field STEM images of threading dislocations that have formed trapped misfit segments in a trapping layer laser ( $g = 002$ ).

## AUTHORS' CONTRIBUTIONS

J.S., J.N., and E.T.H. contributed equally to this work.

Sample growth was supported by the ARPA-E, U.S. Department of Energy, under Award No. DE-AR00000843. This study is based upon the work supported by the National Science Foundation Graduate Research Fellowship under Grant No. 1650114. Further support was provided by the University of California, Santa Barbara Graduate Division through the Doctoral Scholars Program. K.M. acknowledges support from the California Nanosystems Institute SEED-TECH program. The research reported here made use of shared facilities of the UCSB MRSEC (No. NSF DMR 1720256), a member of the Materials Research Facilities Network. The authors are grateful to Arthur C. Gossard, Rushabh Shah, and Mario Dumont for the helpful discussions. The authors have filed a provisional patent application on this work.

## DATA AVAILABILITY

The data that support the findings of this study are available from the corresponding author upon reasonable request.

## REFERENCES

- A. Y. Liu and J. Bowers, *IEEE J. Sel. Top. Quantum Electron.* **24**, 1 (2018).
- T. Egawa, Y. Hasegawa, T. Jimbo, and M. Umeno, *Appl. Phys. Lett.* **67**, 2995 (1995).
- O. Ueda, *Jpn. J. Appl. Phys., Part 1* **49**, 090001 (2010).
- B. Kunert, Y. Mols, M. Baryshnikova, N. Waldron, A. Schulze, and R. Langer, *Semicond. Sci. Technol.* **33**, 093002 (2018).
- Z. I. Kazi, P. Thilakan, T. Egawa, M. Umeno, and T. Jimbo, *Jpn. J. Appl. Phys., Part 1* **40**, 4903 (2001).
- M. E. Groenert, A. J. Pitera, R. J. Ram, and E. A. Fitzgerald, *J. Vac. Sci. Technol., B* **21**, 1064 (2003).
- O. Ueda, *Mater. Sci. Eng. B* **20**, 9 (1993).
- Y. Hasegawa, T. Egawa, T. Jimbo, and M. Umeno, *Jpn. J. Appl. Phys., Part 1* **35**, 5637 (1996).
- M. Yamaguchi, A. Yamamoto, M. Tachikawa, Y. Itoh, and M. Sugo, *Appl. Phys. Lett.* **53**, 2293 (1988).
- I. George, F. Becagli, H. Y. Liu, J. Wu, M. Tang, and R. Beanland, *Semicond. Sci. Technol.* **30**, 114004 (2015).
- D. Jung, P. G. Callahan, B. Shin, K. Mukherjee, A. C. Gossard, and J. E. Bowers, *J. Appl. Phys.* **122**, 225703 (2017).
- J.-M. Gerard and C. Weisbuch, U.S. patent 5075742 A (24 December 1991).
- Z. Mi, P. Bhattacharya, J. Yang, and K. P. Pipe, *Electron. Lett.* **41**, 742 (2005).
- T. Wang, H. Liu, A. Lee, F. Pozzi, and A. Seeds, *Opt. Express* **19**, 11381 (2011).
- A. Y. Liu, C. Zhang, J. Norman, A. Snyder, D. Lubyshev, J. M. Fastenau, A. W. K. Liu, A. C. Gossard, and J. E. Bowers, *Appl. Phys. Lett.* **104**, 041104 (2014).
- S. Chen, W. Li, J. Wu, Q. Jiang, M. Tang, S. Shutts, S. N. Elliott, A. Sobiesierski, A. J. Seeds, I. Ross, P. M. Smowton, and H. Liu, *Nat. Photonics* **10**, 307 (2016).
- J. Kwoen, B. Jang, J. Lee, T. Kageyama, K. Watanabe, and Y. Arakawa, *Opt. Express* **26**, 11568 (2018).
- Z. Liu, C. Hantschmann, M. Tang, Y. Lu, J.-S. Park, M. Liao, S. Pan, A. Sanchez, R. Beanland, M. Martin, T. Baron, S. Chen, A. Seeds, R. Penty, I. White, and H. Liu, *J. Lightwave Technol.* **38**, 240 (2020).
- A. Y. Liu, R. W. Herrick, O. Ueda, P. M. Petroff, A. C. Gossard, and J. E. Bowers, *IEEE J. Sel. Top. Quantum Electron.* **21**, 690 (2015).
- D. Jung, J. Norman, Y. Wan, S. Liu, R. Herrick, J. Selvidge, K. Mukherjee, A. C. Gossard, and J. E. Bowers, *Phys. Status Solidi A* **216**, 1800602 (2019).
- J. Selvidge, J. Norman, M. E. Salmon, E. T. Hughes, J. E. Bowers, R. Herrick, and K. Mukherjee, *Appl. Phys. Lett.* **115**, 131102 (2019).
- R. Beanland, D. J. Dunstan, and P. J. Goodhew, *Adv. Phys.* **45**, 87 (1996).
- D. J. Dunstan, *J. Mater. Sci.* **8**, 337 (1997).
- M. E. Groenert, C. W. Leitz, A. J. Pitera, V. Yang, H. Lee, R. J. Ram, and E. A. Fitzgerald, *J. Appl. Phys.* **93**, 362 (2003).
- H.-C. Luan and L. C. Kimerling, U.S. patent 6635110B1 (21 October 2003).
- E. T. Hughes, R. D. Shah, and K. Mukherjee, *J. Appl. Phys.* **125**, 165702 (2019).
- R. Beanland, J. P. R. David, and A. M. Sanchez, *J. Appl. Phys.* **104**, 123502 (2008).
- I. Yonenaga and K. Sumino, *J. Appl. Phys.* **80**, 3244 (1996).
- I. Yonenaga, K. Sumino, G. Izawa, H. Watanabe, and J. Matsui, *J. Mater. Res.* **4**, 361 (1989).
- J. C. Mikkelsen and J. B. Boyce, *Phys. Rev. B* **28**, 7130 (1983).
- E. B. Yakimov, P. S. Vergeles, A. Y. Polyakov, I.-H. Lee, and S. J. Pearton, *Jpn. J. Appl. Phys., Part 1* **55**, 05FM03 (2016).
- P. G. Callahan, B. B. Haidet, D. Jung, G. G. E. Seward, and K. Mukherjee, *Phys. Rev. Mater.* **2**, 081601 (2018).
- K. Maeda and S. Takeuchi, *Appl. Phys. Lett.* **42**, 664 (1983).
- K. Maeda, M. Sato, A. Kubo, and S. Takeuchi, *J. Appl. Phys.* **54**, 161 (1983).
- C. J. Humphreys, *Rep. Prog. Phys.* **42**, 1825 (1979).
- J. C. Norman, Z. Zhang, D. Jung, C. Shang, M. Kennedy, M. Dumont, R. W. Herrick, A. C. Gossard, and J. E. Bowers, *IEEE J. Quantum Electron.* **55**, 1 (2019).
- D. Jung, R. Herrick, J. Norman, K. Turnlund, C. Jan, K. Feng, A. C. Gossard, and J. E. Bowers, *Appl. Phys. Lett.* **112**, 153507 (2018).
- C. Shang, J. Selvidge, E. Hughes, J. C. Norman, A. A. Taylor, A. C. Gossard, K. Mukherjee, and J. E. Bowers, "A pathway to thin GaAs virtual substrate on on-axis Si (001) with ultralow threading dislocation density," *Phys. Status Solidi A* (published online, 2020).